Advances in Design of High-Performance Heterostructured Scintillators for Time-of-Flight Positron Emission Tomography

Philip Krause, Edith Rogers, and Gregory Bizarri*

Core to advancing time-of-flight positron emission tomography (ToF-PET) toward a less invasive, more flexible procedure with a higher diagnostic power is the development of enhanced radiation detector materials. One promising avenue is the development of heterostructured scintillators where multiple materials work in synergy to exceed the performance of each individual component. Applied to ToF-PET detectors, one component contributes predominantly to the absorption of gamma rays and the other to the creation of ultra-fast photons. Whilst other authors have proposed various concepts, heterostructured scintillators are still in their infancy and scientifically guiding their development remains a challenge. Toward this aim and based on simulation and modeling developments, heterostructure properties are directly linked to ToF-PET performance. This is made possible by redefining the notions of detector photo-peak efficiency and timing response, as defined for monolithic detectors, in the context of heterostructured scintillators. Their overall potential is then discussed as a function of the materials and design used. This provides a quantitative framework to rapidly and efficiently support the advancement of heterostructured detectors for ToF-PET technology.

1. Introduction

The concept of heterostructured radiation detectors has recently been proposed as a possible way to bypass the intrinsic limitations of current radiation detectors[1–9] and reach unprecedented performance (i.e., ref. [10]). The approach—in which multiple materials work in synergy as opposed to a single material trying to fulfill all the needs (for different material discovery/engineering strategies see, for instance refs. [11–19])—has gained traction for its inherent flexibility in tailoring the detector's performance to the application's needs. The drawback of this versatility is the

P. Krause, E. Rogers, G. Bizarri
School of Aerospace, Transport and Manufacturing
Cranfield University
Cranfield, Bedfordshire MK43 0AL, UK
E-mail: gregory.a.bizarri@cranfield.ac.uk

The ORCID identification number(s) for the author(s) of this article can be found under https://doi.org/10.1002/adts.202300425

extent of the parameter space that needs to be surveyed and optimized (material choice and compatibility, assembly, design type, and geometry). This has, if not impeded, then slowed down the development of these detectors.

The requirements are even more exact when applied to time-of-flight positron emission tomography (ToF-PET) detector development, where the properties to optimize, stopping power, and creation of photons emitted at ultra-short time, due to the low stopping power of the currently available fast emitter scintillators, have an anti-correlated character against the heterostructure parameters: the maximization (minimization) of the equivalent stopping power leads to the minimization (maximization) of the number of fast photons (i.e., ref. [7]). The joint optimization of these properties requires a detailed understanding of: 1) the individual scintillation mechanism of each heterostructure material; 2) the impact of each heterostructure component on the performance of the other one; and 3) the impact of the overall heterostructure performance on the application specific performance. Whilst the first two have been discussed by several authors (i.e., refs. [4–7]), the third is largely unknown.

Here, we present an overall simulation and modeling framework linking the heterostructure's design and geometry to ToF-PET performance. The approach, as for the one developed for monolithic detectors (i.e., refs. [20–22]), relies on the redefinition of photo-peak efficiency and timing response in the heterostructure context. Unlike the single material approach, these properties are not uniquely defined by the choice of materials but are dependent on the statistical concept of energy partition, energy absorbed by each detector component for a single gamma ray event. The introduction of these statistical concepts allows for the establishment of a figure of merit (FOM) linking heterostruture properties to ToF-PET performance. This, in turn, provides a quantitative framework (simulation and modeling) to efficiently tailor the heterostructure design for improved ToF-PET performance.

2. Statistical Concepts of Stopping Power and Time Response

For monolithic scintillators, a FOM linking detector properties to ToF-PET performance exists. It is primarily dependent on the

**ADVANCED
SCIENCE NEWS**

www.advancedsciencenews.com

**ADVANCED
THEORY AND
SIMULATIONS**

www.advtheorysimul.com

attenuation length of the material and the coincidence timing resolution (CTR) between the detection of two simultaneous 511 keV events[21]

$$\text{FOM} \simeq \frac{E^2}{\text{CTR}} \qquad (1)$$

where E^2 is the joint photo-peak efficiency for detecting both annihilation photons and (2) 1/CTR accounts for the variance reduction factor (see for instance ref. [20]). A CTR value can be estimated from the light output and time response of the material, $\propto (\frac{\tau_{\text{decay}}\tau_{\text{rise}}}{N})^{0.5}$ with N the absolute light output, for example, the number of photons reaching the photodetector. For monolithic detectors, the FOM is unity for whole-body PET using Lu_2SiO_5:Ce^{3+} (LSO) without TOF information.

To apply a similar approach to heterostructured detectors, the photo-peak efficiency and the coincidence timing resolution need to be redefined in the context of a detector presenting multiple components and materials.

2.1. Equivalent Stopping Power

The ability of a heterostructure to stop and convert gamma rays as a function of the design parameters was presented in detail by P. Krause et al.[7]

The main characteristics are: 1) The equivalent stopping power, defined as the mean of the number of fully absorbed gamma rays over the total number of incoming gamma rays spanned over the front face of the detector, is uniquely defined when the materials and geometry of the heterostructure are fixed; and 2) the equivalent stopping power is almost uniquely governed by the filler volume contribution, regardless of the design studied and the filler materials chosen.

The unicity and properties of the equivalent stopping power allow for its use as a photo-peak efficiency approximation for heterostructured detectors.

2.2. Equivalent Coincidence Timing Resolution

The determination of a CTR for heterostructure scintillators is not straightforward. Several properties have to be accounted for:

i) The intricate emission kinetics of each material, both in terms of the number of components (i.e., Table S1, Supporting Information) and fundamental processes (i.e., crossluminescence emission versus lanthanide emission);
ii) The presence of multiple materials and therefore of multiple timing response contributions;
iii) The event to event variation of the deposited energy partition, and in turn created and emitted photons.

To account for these specificities and establish an analogous time stamp as CTR for heterostructure scintillators, we follow and expand the approach discussed by Tamulaitis et al.[23] In their article, the authors estimated the time resolution of a single monolithic detector with multiple luminescence kinetic components by calculating the detection time, $< t_{ts} >$, needed to detect $N_{\text{threshold}}$ photons, the photon detection threshold (**Figure 1**).
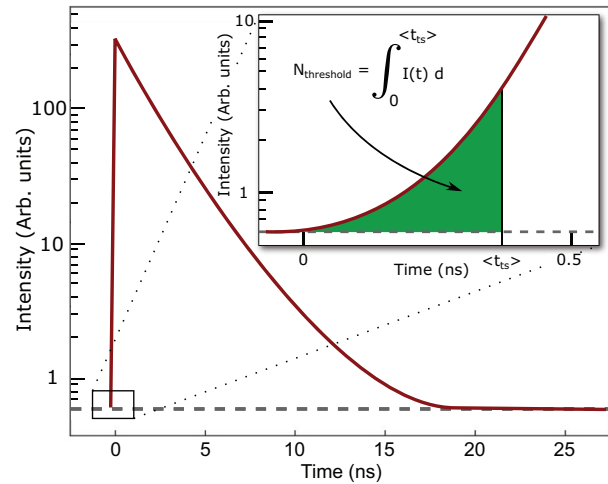

Figure 1. Relationship between the emission intensity, $I(t)$, the mean time, $< t_{ts} >$, and the photon detection threshold $N_{\text{threshold}}$.

This approach is extended here to heterostructured scintillators by extracting the detection mean time event per event based on the reconstruction of the emission intensity, $I(t)$. The latter varies from event to event, and so does $I(t)$ leading to the statistical concepts of $I_i(t)$ and in turn, $< t_{ts}^i >$ where i refers to a specific gamma-ray event.

Extended to a large number of events, this creates a single distribution of detection times which, in turn, allows for a statistical description of each heterostructure time response. A unique descriptor of the timing performance of the heterostructure is then extracted by evaluating:

i) The mean of the entire $< t_{ts}^i >$ distribution, $< \overline{t_{ts}^i} >_{\text{all}}$. This approach is equivalent to providing an equal weight during the image reconstruction to all the fully absorbed events detected. This is the standard approach currently used in PET image reconstruction.
ii) The mean of the $< t_{ts}^i >$ distribution of the shared events, $< \overline{t_{ts}^i} >_{\text{shared}}$. This approach is equivalent to favoring the shared events for the image reconstruction.

In the majority of the cases, both approaches provide a different timing characteristic of the heterostructure (**Figure 2**; Figure S2, Supporting Information—dashed versus dotted lines). Using $< \overline{t_{ts}^i} >_{\text{all}}$ can underestimate the timing benefit of heterostructured scintillators by not fully leveraging the added timing information of the shared events compared to the standard events (fully absorbed in $Bi_4Ge_3O_{12}$ - BGO). Using $< \overline{t_{ts}^i} >_{\text{shared}}$ can overestimate the timing benefit of heterostructured scintillators by assuming that there are sufficient shared events to reconstruct the PET image. A change in the image reconstruction procedure by weighing differently the standard events and the shared energy events would result in fully benefiting from the added timing information of the shared events without degrading the overall detection efficiency of the scanner.

As discussed by Tamulaitis et al., $N_{\text{threshold}}$ is a key parameter of the procedure and has to be chosen in accordance with signal-to-noise considerations. To select a representative value of $N_{\text{threshold}}$,
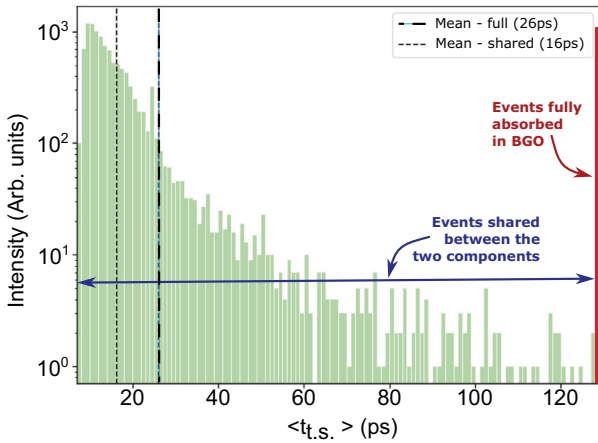
**ADVANCED
SCIENCE NEWS**

www.advancedsciencenews.com

**ADVANCED
THEORY AND
SIMULATIONS**

www.advtheorysimul.com

Figure 2. Example of $< t_{ts}^i >$ distribution for a BGO/BaF$_2$ heterostructure design. The dashed and the dotted lines represent the mean of the $< t_{ts}^i >$ distributions averaged over the total number of events ($< \overline{t_{ts}^i} >_{all}$) and the shared events ($< \overline{t_{ts}^i} >_{shared}$), respectively.

we have simulated the response of monolithic BGO and LSO pixels and determined the detection time for different $N_{threshold}$ values (5, 10, and 15 photons). A value of 10 for $N_{threshold}$ provided the best match between $< t_{ts} >$ and published CTR values (detailed discussion in Section S2.1, Supporting Information).

2.3. Figure of Merit for Heterostructured Detectors

The equivalent stopping power and mean value of the detection time distributions allow the construction of FOMs for the heterostructured scintillators similar to the one established for monolithic detectors (Equation (1)). Due to the statistical nature of the heterostructure timing response, several approaches can be defined for the FOMs of these detectors:

i) Substitution of the CTR value by the mean of the $< t_{ts}^i >$ distributions over all the fully absorbed events and of the photo-peak efficiency by the equivalent stopping power, also raised to the square:

$$FOM_{all} \simeq \frac{ESP^2}{< \overline{t_{ts}^i} >_{all}} \qquad (2)$$

with ESP and $< \overline{t_{ts}^i} >_{all}$, respectively the equivalent stopping power (ESP) and the mean over all the fully absorbed 511 keV events of the detection time distribution. This approach is equivalent to providing an equal weight during the image reconstruction to all the fully absorbed events detected.

ii) Substitution of the CTR value by the mean of the $< t_{ts}^i >$ distributions restricted to the shared events only (gamma-ray events where the absorbed energy is shared between the detector components; see Krause et al.[7]) and of the photo-peak efficiency by the equivalent stopping power normalized to the number of shared events, also raised to the square. This case

corresponds to the rejection of any event fully absorbed in the matrix component of the detector

$$FOM_{shared} \simeq \frac{(ESP * N_{shared})^2}{< \overline{t_{ts}^i} >_{shared}} \qquad (3)$$

with ESP, N_{shared} and $< \overline{t_{ts}^i} >_{shared}$, respectively, the equivalent stopping power, the number of shared events normalized by the number of fully absorbed 511 keV events, and the mean over all the fully absorbed shared events of the mean-time distribution. This approach favors the event with more accurate timing information and shared events, for the image reconstruction.

These two FOMs can be used to evaluate the impact of the design type, filler material, and matrix material on the overall performance of heterostructured scintillators. Overall performance means, in this context, the added value of the detector for the application performance. This is opposed to the evaluation of the individual and intrinsic scintillation performance of each materials. This newly developed FOM, and contrary to the previously developed FOM for monolithic detectors (Equation (1)) results in values of 10.4 and 14.6 for a BGO and LSO:Ce^{3+} monolithic pixels of similar dimensions ($3 \times 3 \times 15$ mm^3), respectively. These values will serve as benchmarks to evaluate the performance of the heterostructured scintillaotrs. Finally, it is also important to note that the FOM$_{all}$ and FOM$_{shared}$ values are identical for monolithic detectors.

3. Application to Heterostructured Detectors Development

3.1. Detection Time Distribution

Based on the reconstruction of the emission intensity for each event, $I_i(t)$, and on the selected photon detection threshold of 10, $N_{threshold}$, a value of $< t_{ts}^i >$ was extrapolated for each simulated event and for each simulated heterostructure design. To survey the design parameter space, several configurations in terms of geometries and materials have been simulated:

i) Two different fiber-based heterostructure design geometries (fiber diameter of 88 µm and pitch of 333 µm and fiber diameter of 119 µm and pitch of 167 µm). The geometries correspond to a small and large pitch/diameter ratio, respectively.
ii) Three types of matrix/filler material combinations (BGO/plastic, BGO/(BA)$_2$PbBr$_4$, and BGO/BaF$_2$). The three filler materials are representative of a low, medium, and high density materials, respectively.

Figure 2 presents an example of $< t_{ts}^i >$ distributions for a BGO/BaF$_2$ fiber-based heterostructure design with a fiber diameter of 119 µm and a pitch of 167 µm. Color coded for each distribution are: 1) a red box corresponding to the number of fully absorbed events when all the energy has been absorbed in the BGO sub-component, no energy transfer between the matrix and the filler; 2) green boxes corresponding to individual $< t_{ts}^i >$ values resulting from fully absorbed events where a part of the energy

**ADVANCED
SCIENCE NEWS**

www.advancedsciencenews.com

**ADVANCED
THEORY AND
SIMULATIONS**

www.advtheorysimul.com

has been deposited in the filler component; and 3) a blue line delineating the range of $< t_{ts}^i >$ values when the energy is shared between the two heterostructure components. The dashed and the dotted line in each graph are the mean of the $< t_{ts}^i >$ distributions averaged over the total number of events ($\overline{< t_{ts}^i >}_{all}$) or the shared events ($\overline{< t_{ts}^i >}_{shared}$), respectively.

In terms of the design parameter impact on the $< t_{ts}^i >$ distributions, the results are similar to those already discussed by Krause et al.[7] (see also Section S3.1, Supporting Information):

i) A reduction of the pitch/diameter ratio promotes the energy exchange between the heterostructure components and, in turn, decreases the number of events fully absorbed in the BGO sub-component.
ii) An increase in the filler material density results in a skew in the distribution of the shared event toward lower detection times. The impact on the events fully absorbed in the BGO component is minimal.

Consequently, the achievable CTR values are spread over a large range depending on the shape of the distribution, the geometry, the method of calculation (mean over the entire event population or over the shared event subpopulation), and the intrinsic properties of the filler material used. The results are mediocre for any configuration with a low energy sharing capability (large pitch/diameter ratio designs) regardless of the method used to calculate the CTR values (CTR values ranging from 115 to 129 ps). However, even when the design presents a high energy sharing ability, the improvement of the CTR values is highly impacted by the stopping power capability, and timing response of the filler component (mediocre for the plastic leading to CTR values of about 125 ps and excellent for the two other materials, leading to CTR values less than 40 ps). As previously mentioned and expected, the method of calculation using only the shared event population leads to lower values of CTR.

3.2. FOM-Based Performance Survey

Figures of merit values, FOM_{all} and FOM_{shared}, have been calculated using Equations (2) and (3) for four sets of heterostructure configurations, each including multiple design geometries. **Figure 3** shows an example of such dependence, FOM_{all} as a function of the filler material for a long axis fiber based BGO heterostructures. The dependence of FOM_{all} and FOM_{shared} on the filler material choice, the matrix material and the geometry are presented and further discussed in Figures S3a, S4a, S5a, and S7, Supporting Information.

i) BGO/plastic heterostructures with four design types: plate- or fiber-based structures both aligned along the short or long axis (Figures S3a and S4a, Supporting Information).
ii) Long axis oriented fiber heterostructures with five different filler materials (Figure 3; Figure S5a, Supporting Information).
iii) Long axis oriented fiber heterostructures with two matrix materials, BGO and LSO, and two filler materials, $(BA)_2PbBr_4$ and BaF_2 (Figure S7, Supporting Information)
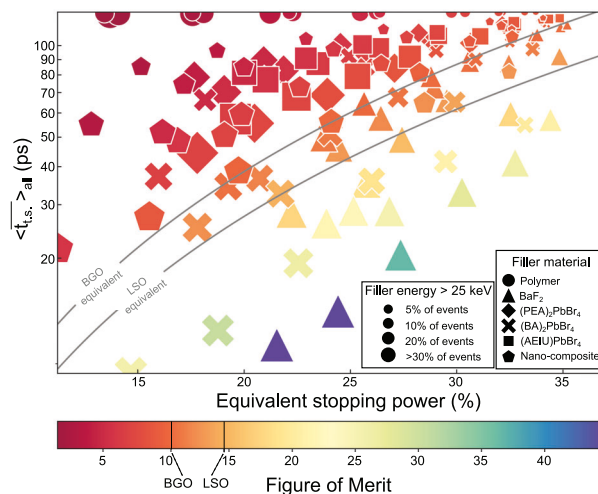

Figure 3. FOM_{all} (color) as a function of the equivalent stopping power (x-axis) and the $\overline{< t_{ts} >}_{all}$ (y-axis) for long axis fiber heterostructure designs (individual marker) with six different filler materials (marker's shape). The size of the marker is associated with the contribution of shared events to the total number of fully absorbed events with at least 25 keV deposited in the filler component.

iv) Long axis oriented fiber heterostructures with BGO/BaF_2 or BGO/$(BA)_2PbBr_4$ where the diameter or the pitch of the geometry have been optimized for the best performance (Figure S8, Supporting Information).

Focusing only on the overall guidance power of the survey, the results can be summarized as:

i) The best achievable FOM values are linked to the long axis aligned plate design type. The long axis fiber based designs have FOM values about 20% lower (e.g., Figure S8, Supporting Information).
ii) For all the configurations studied, the BGO based heterostructures outperformed the LSO ones (e.g., Figure S6, Supporting Information).
iii) The best FOM values are all obtained for configurations with a large filler volume contribution and, in turn, high energy exchange capability (small pitch/diameter ratio, e.g., Figure 3; Figure S5a, Supporting Information). The optimum FOM values are obtained when the benefit of increasing the energy exchange capability by reducing the matrix thickness is outperformed by the inherent decrease of the stopping power associated (e.g., Figure 5d,h). The balance depends on the matrix and filler stopping power values.
iv) The best achievable FOM values increase through the filler material sequence: plastic, $(PEA)_2PbBr_4$, $(AEIU)PbBr_4$, nano-composite, $(BA)_2PbBr_4$, and BaF_2. The trend follows the decrease in the filler materials' attenuation lengths, which impacts positively both the number of fast photons created (energy absorbed in the filler) and the overall equivalent stopping power of the heterostructure.
v) All the filler materials studied with the exception of the plastic scintillator have heterostructure designs where $< t_{ts} >$ values are significantly improved compared to the one obtained

**ADVANCED
SCIENCE NEWS**

www.advancedsciencenews.com

**ADVANCED
THEORY AND
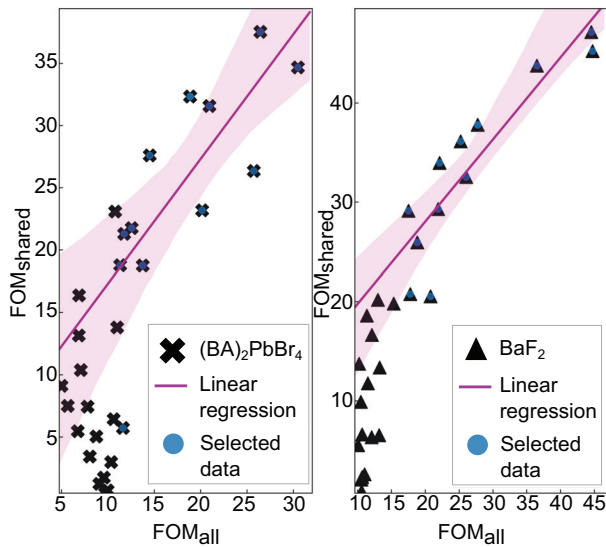SIMULATIONS**

www.advtheorysimul.com

Figure 4. Comparison of the FOM$_{all}$ and FOM$_{shared}$ values for the two best filler materials using BGO as matrix material. The purple line and area are the linear regression line and error, respectively.

for a BGO monolithic pixel. A few configurations reach values as low as 10 ps.

vi) Nano-composite, $(BA)_2PbBr_4$, and BaF_2 have configurations that achieve FOM values significantly better than the value obtained for a monolithic BGO reference pixel (FOM of 10.4). $(BA)_2PbBr_4$ and BaF_2 have designs resulting in FOMs notably higher (40+) than the one obtained for a monolithic LSO reference pixel (FOM of 14.6).

It is important to remember that these results are a reading of the simulation output; hence, they are framed by the simulation own limitations. The main parameters not accounted for in the simulation are the mechanisms associated with the scintillation light, such as transport, extraction, and transfer mechanisms. As such, the guidelines represent an ideal case where any created scintillation photon will reach the light detector and be measured. While these approximations are perfectly acceptable in most cases and do not jeopardize the selection rules for the design geometry and materials, there are also specific drawbacks. This is the case for the configurations using BaF_2 where the fast emission is emitted in the ultra-violet (UV) band. This is problematic as: 1) UV light cannot propagate in BGO (reabsorption), and will be at best re-emitted as a "slow" component and 2) the detection efficiency of UV light is not as high as for a visible emission, resulting in an over estimation of the number of BaF_2 photons detected.

Figure 4 illustrates a more fundamental aspect associated with the use of FOM$_{all}$ and FOM$_{shared}$. For FOM values of interest higher than 10 (monolithic BGO pixel reference) or 15 (monolithic LSO pixel reference), the two FOMs provide similar trends. This demonstrates that both FOM methods can be used to guide the development and performance improvement of heterostructured scintillators for ToF-PET. For FOM values smaller than 10, the results are less correlated, largely due to the lack of energy ex-

change in these configurations, which strongly impacts the overall equivalent stopping power for FOM$_{shared}$.

3.3. Simple Modeling of FOM

While the results presented so far present a comprehensive pathway toward design selection and performance engineering of heterostructured detectors, the efficiency of the method is limited by the need for a time-consuming simulation stage prior to assessment. This section provides a mechanistic modeling approach that allows for a direct assessment of the relationship between performance and design. This approach extends the work published by P. Krause et al., with the modeling of the equivalent stopping power and energy sharing capacity of these detectors as a function of their design geometry and material constituents.[7] Here, the models are further refined and extended to allow for the concurrent evaluation of the equivalent stopping power (ESP), the number of shared events (NSE - N_{shared}), and the detection time distribution mean ($< \overline{t_{ts}} >_{shared}$). These three models allow, in turn, the modeling and quantification of FOM$_{shared}$. Hereafter, the modeling targets the plate-based heterostructure designs. Similar approaches can be made for fiber-based designs.

The models for ESP, NSE, and $< \overline{t_{ts}} >_{shared}$ are established from individual physics-based analytical functions. Each function integrates parameters describing the geometry of the design (matrix and filler thicknesses and length of the pixel) and all or a subset of the physical and scintillation properties of the component materials (radiation lengths, electron ranges, light outputs, and time responses):

i) ESP is derived from a standard equation for the transmitted gamma ray intensity where the unique material is substituted by two materials weighted by their volume fraction

$$ESP = \left(1 - (1-\nu)e^{-\alpha_{matrix}L} - \nu e^{-\alpha_{filler}L}\right)^{p_{ESP}} \quad (4)$$

with L, the pixel length; ν the volume ratio of the filler; and matrix components; α_{matrix} and α_{light}, the attenuation lengths of the matrix and filler, respectively. These values are fixed and determined by the properties of the design. P_{ESP} is the unique parameter used to fit all the ESP data simultaneously.

ii) NSE is approximated by two Gompertz functions describing separately the impact of the matrix and filler thicknesses on the shared events:

$$NSE = \left(1 - e^{-A_{m1}*e^{-A_{m2}*\frac{\delta_{matrix}}{e_{matrix}}}}\right)\left(e^{-A_{f1}*e^{-A_{f2}*\frac{\delta_{filler}-\delta_0}{e_{filler}}}}\right) \quad (5)$$

with δ_{matrix} and δ_{filler}, the matrix and filler thicknesses, respectively; e_{matrix} and e_{filler}, the matrix and filler electron ranges, respectively. A_{m1}, A_{m2}, A_{f1}, A_{f2}, and δ_0 the parameters used to fit all the NSE data simultaneously.

iii) The detection time distribution mean ($< \overline{t_{ts}} >_{shared}$) is derived from the square root ratio between the timing response and the number of fast photons emitted, similar to the estimation of the CTR in a monolithic detector. The number of
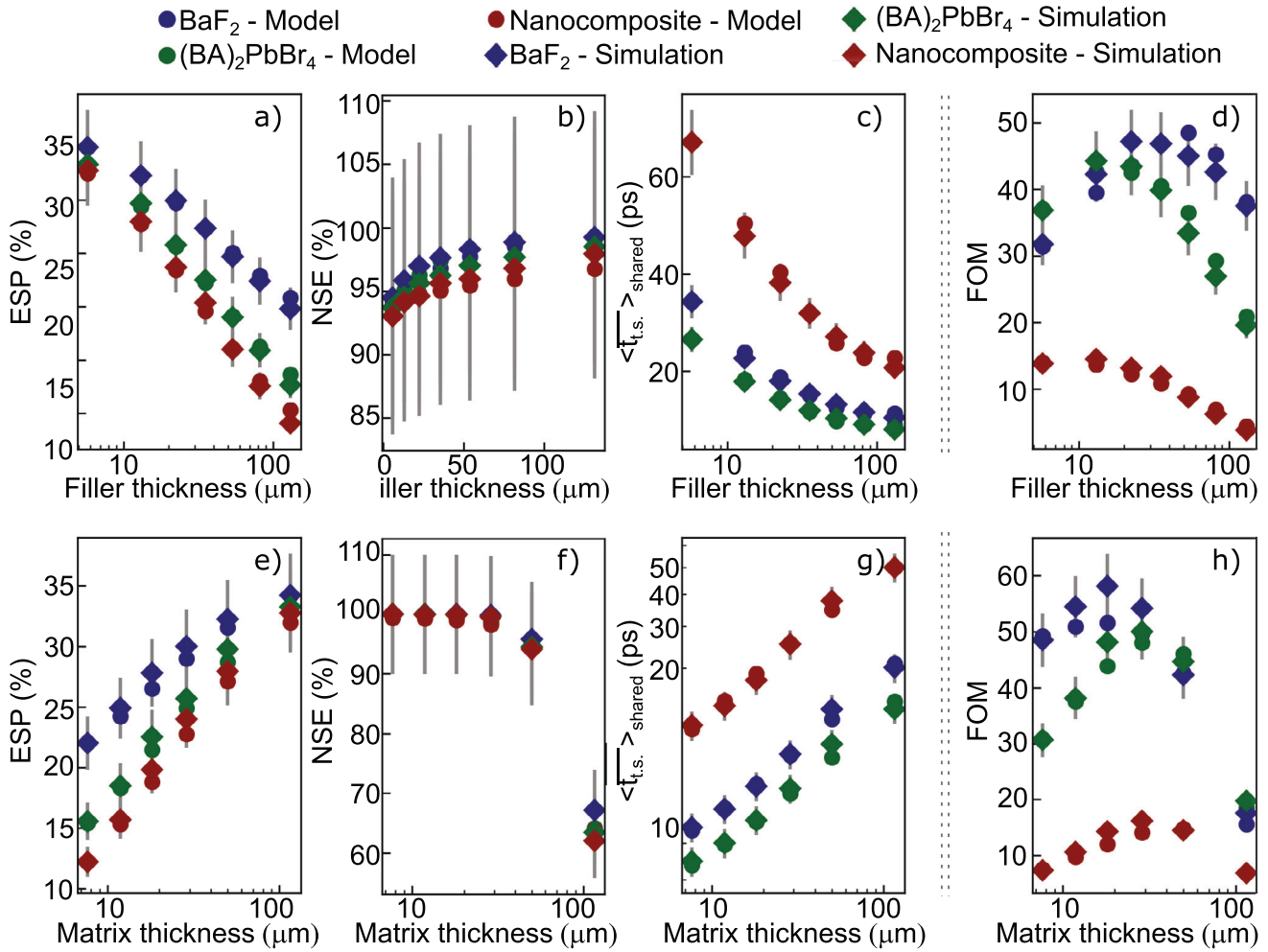
ADVANCED
SCIENCE NEWS

www.advancedsciencenews.com

ADVANCED
THEORY AND
SIMULATIONS

www.advtheorysimul.com

Figure 5. Comparison of simulation and model output data for the equivalent stopping power, number of shared events, mean detection time distribution, and figure of merit for a plate-based heterostructure design. The top graphs show the dependence of the markers against the filler thickness for a fixed matrix thickness (50 µm). The bottom graphs present the same dependencies against the matrix thicknesses for a fixed filler thickness (13 µm). a,e) The equivalent stopping power (ESP) values. b,f) The number of shared events (NSE) values. c,g) The detection time distribution means ($< \overline{t_{ts}} >_{\text{shared}}$) values. d,h) The non simulated figure of merit values resulting from the convolution of ESP, NSE, and $< \overline{t_{ts}} >_{\text{shared}}$ according to Equation (3).

fast photons is calculated by taking the mean over the initial position of the recoil electron of the energy deposited in the structure (geometric criteria and electron ranges of components—additional document) and accounting for the light outputs and timing response distributions of the detector constituents:

$$
< \overline{t_{ts}} >_{\text{shared}} = \left[\left(\overline{\delta E_{\text{matrix}} LO_{\text{matrix}} \sum_i^{\text{matrix}} \frac{\delta t_i}{\tau_{\text{decay}_i} \tau_{\text{rise}_i}}} \right) \right.
$$

$$
\left. + \left(\overline{\delta E_{\text{filler}} LO_{\text{filler}} \sum_j^{\text{filler}} \frac{\delta t_j}{\tau_{\text{decay}_j} \tau_{\text{rise}_j}}} \right) \right]^{-\frac{1}{2}}
$$

(6)

with $\delta E_{\text{matrix or filler}}$, the energy absorbed in the matrix (filler) component. The value depends on how far the recoil electron

(electron travel distance) can travel within the heterostructure (geometry) and the number and emission kinetic of the created photons when crossing the detector components ($LO_{\text{matrix or filler}}$, the light output of the matrix (filler) material; $\delta t_{i \text{ or } j}$, the contribution to the matrix (filler) light output of each time response components; $\tau_{\text{decay}_{i \text{ or } j}}$, $\tau_{\text{rise}_{i \text{ or } j}}$, and the rise time of each matrix (filler) component). There are no additional fitting parameters.

These analytical forms are then used as fitting functions to simultaneously best reproduce the entire set of simulated data (simulated and model output data in **Figure 5**a,b,c,e,f,g; raw data for FOM$_{\text{shared}}$ in Figure S8, Supporting Information). These data correspond to the dependence of ESP, NSE, and $< \overline{t_{ts}} >_{\text{shared}}$ for a long axis fiber based design against the filler thickness for a constant matrix thickness (circles in upper graphs), against the matrix thickness for a constant filler thickness (circles in lower
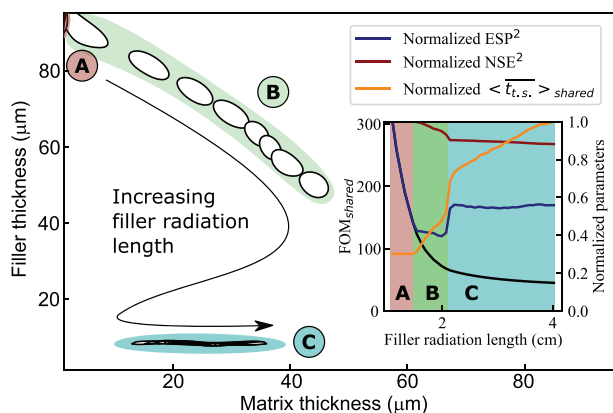
**ADVANCED
SCIENCE NEWS**

www.advancedsciencenews.com

**ADVANCED
THEORY AND
SIMULATIONS**

www.advtheorysimul.com

Figure 6. 2D mapping of the best FOM values obtained as a function of matrix and filler thicknesses and for different filler material radiation lengths. The data have been obtained by fixing the matrix material to BGO and the filler material to a hypothetical scintillator with the properties of $(BA)_2PbBr_4$ with the exception of the radiation length which varies. The inset presents the normalized FOM_{shared}, NSE^2, and $< \overline{t_{ts}} >_{shared}$ as a function of the attenuation length.

graphs), and as a function of the filler materials (blue markers for BaF_2, red markers for nanocomposite, and green markers for $(BA)_2PbBr_4$). The fitting procedure, the least squares method, was done simultaneously across all of the data. The known physical properties (light outputs, time responses, BaF_2 attenuation length, matrix or filler thicknesses, and pixel length) were kept constant, whilst all the unknown parameters were constrained to a single value across the entire dataset (electron ranges, $(BA)_2PbBr_4$ and nanocomposite attenuation lengths). The other parameters, P_{ESP}, A_{1m}, A_{2m}, A_{1f}, A_{2f}, and δ_0 were left free. The goodness of the fit can be seen across the entire dataset (diamond markers—Figure 5; the error bars correspond to a 10% error), but also when comparing the simulated data of FOM_{shared} to the convolution of the three functions to recreate an independent analytical function to evaluate the FOM values (insets (d,h) with a consistent marker's color and shape code). Details of the output fitting parameters are reported in Tables S2–S4, Supporting Information, though it is important to underline the coherence and correctness of the parameters associated with real physical properties such as electron lengths (i.e., 90 µm for the fitting procedure compared to 85 µm from the simulated value) or radiation lengths (3 and 3.9 cm for $(BA)_2PbBr_4$ and nanocomposite; BaF_2 published value is 2.02 cm[24]).

This modeling approach allows you to extrapolate beyond the initial parameter space studied and to further assess the individual impact of each heterostructure property on the overall performance of a ToF-PET scanner. **Figure 6** shows an overview of the dependence of the FOM on the radiation length of the filler material when all the other parameters are kept constant (value associated with a $BGO/(BA)_2PbBr_4$ long fiber based pixel). The main graph presents the best design configurations as a function of the matrix and filler thicknesses when the radiation length of the filler material varies. The inset shows the individual dependencies of the FOM, ESP, NSE, and $< \overline{t_{ts}} >_{shared}$ as a function of the filler attenuation length for these designs. These results show that the FOM of a heterostructure detector

could theoretically reach values as high as several hundreds, about twenty times higher than that of an LSO monolithic pixel of similar dimensions. However, these designs have currently limited practical implications as these FOM values are linked to filler materials with an attenuation length comparable to the one of BGO. Stated differently, if such materials existed, a short attenuation length with scintillation properties similar to those of $(BA)_2PbBr_4$, the need for heterostructured scintillators will be, if not null, then limited. In terms of optimum designs, these configurations, area A in main Figure 6 (attenuation length up to 1.5 cm), tend to minimize the overall matrix volume to favor the creation of fast photons in the filler component. This is also seen in the inset of Figure 6. In this range, the decrease of FOM values is associated with a decrease of ESP, while $< \overline{t_{ts}} >_{shared}$ values remain stable. In area B (attenuation lengths up to 2 cm), the degradation of the ESP becomes too impactful on the overall detector performance, and the nature of the optimum design changes to one that mitigates the decrease of the ESP. The best geometries tend to increase the matrix contribution to the overall detector volume. To minimize the impact on the detector performance, ESP is now favored over the creation of fast photons, as seen in the increase of the $< \overline{t_{ts}} >_{shared}$ values. Area C (attenuation length up to 4 cm) presents similar but exacerbated behavior, where the contribution of the filler component is greatly minimized to maximize the ESP values. This leads to designs with extremely small dimensions for both the matrix and filler thicknesses.

The impact of other properties such as the matrix material attenuation length and the matrix or filler material recoil electron travel distance have also been studied (Figures S9–S11, Supporting Information). It is shown that the detector performance is also extremely sensitive to the matrix attenuation length and that values departing from the ones of BGO or LSO (greater than 1.5 cm) will lead to a heterostructured scintillator with worse performance than an equivalent monolithic LSO pixel. The electron ranges of materials are difficultly tunable, but if they were, the detector performance would be maximized by minimizing the filler material electron range while maximizing one of the matrix components. The latter favors the energy exchange between the two components, which in turn maximizes the capability of the heterostructure to share the absorbed energy.

3.4. Conclusions and Detector Development Guidelines

This work proposes an overall simulation and modeling framework for the design of high-performance heterostructured scintillators for their application in ToF-PET imaging. While the approach has its intrinsic limitations—for example, no light transport is accounted for in the model—it also allows us a direct comparison and quantification of the detector performance for various geometries, types, and material configurations. Based on the analytical form of the FOM, several guiding principles can be instanced:

i) Heterostructured scintillators can theoretically supersede the monolithic detector in terms of performance. Depending on the design and the matrix/filler materials chosen, the achievable improvement ranges from two to several

ADVANCED
SCIENCE NEWS

www.advancedsciencenews.com

ADVANCED
THEORY AND
SIMULATIONS

www.advtheorysimul.com

tens of times the performance of standard ToF-PET LSO scintillators. The factor of improvement for the ToF-PET performance would follow similar numbers.

ii) The best design type is always linked to the long-axis plate geometry. The long-axis fiber design FOMs are about 20% lower than the previous geometries.

iii) The best designs are systematically associated with high energy exchange geometries, which depending on the properties of the matrix and filler materials are often associated with small thicknesses of the two components. Quantitatively and realistically, this corresponds to a plate design with thicknesses lower than 50 μm for the matrix and 80 μm for the filler and a fiber design with thicknesses lower than 50 μm for the matrix and 150 μm for the filler.

iv) While ideally the filler radiation length should be as high as possible, the current available fast emitter materials are all mediocre in this matter. The downselection among those materials should strongly favor scintillators with an attenuation length smaller than 3 cm to be able to compete with the current detector technology.

v) In terms of matrix attenuation length, the choice of material should focus on scintillators with an attenuation length as close as possible to the ones of BGO and LSO (1.1 cm). Departing from these values, for example, above 1.5 cm, leads to a drastic decrease in the detector performance.

vi) The recoil electron travel distances, if one could engineer them, should be maximized and minimized for the matrix and filler materials, respectively.

While this study presents a set of guidelines that if followed, should help in developing high performance heterostructured scintillators for the next generation of ToF-PET technology, it is also important to underline other properties and performance markers that were not discussed or accounted for in this study.

3.4.1. Light Yield and Time Response of Materials

While the scintillation performance of the materials was used to quantify the FOM of each heterostructure configuration (Table S1, Supporting Information), an independent discussion of the impact of the light yield and time response on the FOM was not. A detailed study is outside the scope of this article; however, it is already possible to draft some quantitative guidelines from the simple modeling of the FOM (Equations (3)–(6)). The dependence of the materials' scintillation properties on the FOM is uniquely present in Equation (6) and can, at first, be approximated by $\sqrt{\frac{LO}{\tau_{decay}\tau_{rise}}}$, similar to the formula developed for monolithic scintillators. Contextualized in the selection of a filler material, the best BGO/plastic designs (Figure S3a, Supporting Information) could only compete with an LSO monolithic pixel if the scintillation performance of the plastic scintillator, keeping the other properties constant, was improved by a factor of more than 40. The factor of 40 represents either an improvement in the light output or a decrease in the time response, or a mix of both (time density of photons).

3.4.2. Light Transport/Extraction Efficiencies

The presence of multiple domains is expected to degrade light transport and extraction efficiencies. This is due to the increase in complexity of the optical paths but also to the possibility of optical cross talk between the different components, the latter leading to light loss (reabsorption) and time delay. While experimental assessments of the impact are currently done in various laboratories, engineering solutions (i.e., photonic structures) allowing better control of light transport and extraction are also being developed in parallel (i.e., refs. [25, 26]). It is expected that these approaches should help mitigate the overall degradation of the heterostructure light yield.

3.4.3. Energy Resolution of a Multi-Component Detector

Here, also a degradation of the performance is expected. The intrinsic energy sharing mechanism of a heterostructure detector leads to an event-to-event non-uniform response in terms of light output. This in turn should lead to a degradation of the energy resolution due to the difference in light outputs of the two materials. While the first experimental results do not indicate a significant degradation, the impact will have to be carefully quantified as the potential consequences on the performance of ToF-PET reconstruction, in particular Compton scattered event rejection, could be a serious roadblock to heterostructured scintillator development. It is, however, interesting to notice that the best designs proposed in this article are all related to high energy sharing ability, almost close to 100%. If such values are experimentally achievable, the impact of the heterostructured nature of the detector on the energy resolution should be, if not negligible, greatly mitigated.

As a concluding remark, it is remarkable to see that even with the current technology and materials, the heterostructure approach should be able to supersede the standard monolithic approach as a ToF-PET detector. While polymer (low density) or BaF$_2$ (UV emission) designs currently present some prohibitive drawbacks, (BA)$_2$PbBr$_4$ configurations, keeping in mind the technical challenges associated with their manufacture, seem to have the sought for well-balanced properties to demonstrate the possible game changing aspects of heterostructured detectors.

Supporting Information

Supporting Information is available from the Wiley Online Library or from the author.

Acknowledgements

Conflict of Interest

The authors declare no conflict of interest.

[1] C. Dujardin, E. Auffray, E. Bourret-Courchesne, P. Dorenbos, P. Lecoq, *IEEE Trans. Nucl. Sci.* **2018**, *65*, 1977.

[2] R. M. Turtos, S. Gundacker, E. Auffray, P. Lecoq, *Phys. Med. Biol.* **2019**, *64*, 185018.

[3] P. Lecoq, C. Morel, J. O. Prior, D. Visvikis, S. Gundacker, E. Auffray, P. Križan, R. M. Turtos, D. Thers, E. Charbon, J. Varela, C. de La Taille, A. Rivetti, D. Breton, J.-F. Pratte, J. Nuyts, S. Surti, S. Vandenberghe, P. Marsden, K. Parodi, J. M. Benlloch, M. Benoit, *Phys. Med. Biol.* **2020**, *65*, 21RM01.

[4] F. Pagano, N. Kratochwil, M. Salomoni, M. Pizzichemi, M. Paganoni, E. Auffray, *Phys. Med. Biol.* **2022**, *67*, 135010.

[5] P. Lecoq, G. Konstantinou, R. Latella, L. Moliner, J. Nuyts, L. Zhang, J. Barrio, J. M. Benlloch, A. J. Gonzalez, *IEEE Trans. Radiat. Plasma Med. Sci.* **2022**, *6*, 510.

[6] G. Konstantinou, P. Lecoq, J. M. Benlloch, A. J. Gonzalez, *IEEE Trans. Radiat. Plasma Med. Sci.* **2022**, *6*, 5.

[7] P. Krause, E. Rogers, M. D. Birowosuto, Q. Pei, E. Auffray, A. N. Vasil'ev, G. Bizarri, *Heliyon* **2022**, *8*, e09754.

[8] P. Mohr, N. Efthimiou, F. Pagano, N. Kratochwil, M. Pizzichemi, C. Tsoumpas, E. Auffray, K. Ziemons, *IEEE Trans. Radiat. Plasma Med. Sci.* **2023**, *7*, 41.

[9] E. G. Rogers, M. D. Birowosuto, F. Maddalena, C. Dujardin, F. Pagano, N. Kratochwil, E. Auffray, P. Krause, G. Bizarri, *Appl. Phys. Lett.* **2023**, *122*, 081901.

[10] The 10ps Challenge; A Step Toward Reconstruction-Less TOF-PET, https://the10ps-challenge.org/ (accessed: September 2023).

[11] I. Moreels, *Nat. Mater.* **2015**, *14*, 464.

[12] J. Perego, I. Villa, A. Pedrini, E. C. Padovani, R. Crapanzano, A. Vedda, C. Dujardin, C. X. Bezuidenhout, S. Bracco, P. E. Sozzani, A. Comotti, L. Gironi, M. Beretta, M. Salomoni, N. Kratochwil, S. Gundacker, E. Auffray, F. Meinardi, A. Monguzzi, *Nat. Photonics* **2021**, *15*, 393.

[13] A. Xie, F. Maddalena, M. E. Witkowski, M. Makowski, B. Mahler, W. Drozdowski, S. V. Springham, P. Coquet, C. Dujardin, M. D. Birowosuto, C. Dang, *Chem. Mater.* **2020**, *32*, 8530.

[14] Y. Liu, H. Zang, L. Wang, W. Fu, W. Yuan, J. Wu, X. Jin, J. Han, C. Wu, Y. Wang, H. L. Xin, H. Chen, H. Li, *Chem. Mater.* **2016**, *28*, 7537.

[15] S. E. Derenzo, B.-E. Courshesne, G. Bizarri, A. Canning, *Nucl. Instrum. Methods Phys. Res., Sect. A* **2016**, *805*, 36.

[16] Y. Liu, W. Yuan, Y. Shi, X, Chen, Y, Wang, H. Chen, H. Li, *Angew. Chem., Int. Ed.* **2014**, *53*, 4127.

[17] X. Zhang, H. Qiu, W. Luo, K. Huang, Y. Chen, J. Zhang, B. Wang, D. Peng, Y. Wang, K. Zheng, *Adv. Sci.* **2023**, *10*, 2207004.

[18] S. Derenzo, E. Bourret, S. Hanrahan, G. Bizarri, *J. Appl. Phys.* **2018**, *123*, 114501.

[19] M. Gascon, E. C. Samulon, G. Gundiah, Z. Yan, I. V. Khodyuk, S. E. Derenzo, G. A. Bizarri, E. D. Bourret-Courchesne, *J. Lumin.* **2014**, *156*, 63.

[20] T. Budinger, S. Derenzo, G. Gullberg, W. Greenberg, R. Huesman, *J. Comput. Assisted Tomogr.* **1977**, *1*, 131.

[21] S. E. Derenzo, W. S. Choong, W. W. Moses, *Phys. Med. Biol.* **2015**, *60*, 7309.

[22] M. Conti, B. Bendriem, *Clin. Transl. Imaging* **2019**, *7*, 139.

[23] G. Tamulaitis, A. Vasil'ev, M. Korzhik, A. Mazzi, A. Gola, S. Nargelas, A. Vaitkevičius, A. Fedorov, D. Kozlov, *IEEE Trans. Nucl. Sci.* **2019**, *66*, 1879.

[24] Advatech, *Radiation Detectors Scintillator - BaF$_2$ Properties*, https://www.advatech-uk.co.uk/baf2.html (accessed: October 2023).

[25] X. Lin, H. Hu, S. Easo, Y. Yang, Y. Shen, K. Yin, M. P. Blago, I. Kaminer, B. Zhang, H. Chen, J. Joannopoulos, M. Soljacic, Y. Luo, *Nat. Commun.* **2021**, *12*, 5554.

[26] W. Ye, G. Bizarri, M. D. Birowosuto, L. J. Wong, *ACS Photonics* **2022**, *9*, 3917.

2023-10-10

Advances in design of high-performance heterostructured scintillators for time-of-flight positron emission tomography

Krause, Philip George

Wiley